



## Remote sensing of ionospheric disturbances associated with energetic particle precipitation using the South Pole VLF beacon

M. W. Chevalier,<sup>1</sup> W. B. Peter,<sup>1</sup> U. S. Inan,<sup>1</sup> T. F. Bell,<sup>1</sup> and Maria Spasojevic<sup>1</sup>

Received 27 March 2007; revised 30 June 2007; accepted 26 July 2007; published 16 November 2007.

[1] The Stanford University VLF beacon transmitter located at South Pole operates at 19.4 kHz, transmitting for 1 min intervals every 15 min throughout the day. The beacon serves as a tool to measure changes in the *D* region ionospheric conductivity owing to energetic particle precipitation and is capable of providing coverage that spans the Antarctic continent. We present VLF beacon signal amplitude and phase data measured at Palmer Station, Antarctica. Diurnal and seasonal variations are discussed first, followed by analysis of data from two periods of high geomagnetic activity, in July 2004 and in May 2005, with a phase advance and an amplitude depression of the beacon signal (as recorded at Palmer) observed for both cases. Data from the MEPED instrument aboard the NOAA-16 and 17 POES satellites show an increase in energetic electron (>100 keV) and proton (>16 MeV) precipitation fluxes coincident with the VLF beacon signal perturbations. The fluxes measured on POES are used as an aide to generate profiles of secondary ionization along the great circle path from South Pole to Palmer. These profiles are then applied to a quantitative model of subionospheric VLF signal propagation to estimate the phase and amplitude variations expected. Results indicate that the observed VLF amplitude and phase data are in reasonable agreement with theoretical calculations in both cases, indicating that the model captures the ionospheric disturbance in effect during both of the disturbed periods.

**Citation:** Chevalier, M. W., W. B. Peter, U. S. Inan, T. F. Bell, and M. Spasojevic (2007), Remote sensing of ionospheric disturbances associated with energetic particle precipitation using the South Pole VLF beacon, *J. Geophys. Res.*, *112*, A11306, doi:10.1029/2007JA012425.

### 1. Introduction

[2] The flux of energetic electrons (>100 keV) in the outer radiation belts ( $3 < L < 7$ ) typically exhibit dramatic increases during geomagnetic storms. For relativistic (>1 MeV) electrons, the fluxes can vary by up to two orders of magnitude on the timescale of a few hours to days [Paulikas and Blake, 1979; Baker et al., 1986]. One of the primary loss mechanisms for both energetic and relativistic electrons is precipitation into the upper atmosphere [e.g., Green et al., 2004]. Precipitation may result from pitch angle scattering owing to increased field line curvature as well as interactions with plasma waves such as electron cyclotron harmonic (ECH) waves [Horne and Thorne, 2000], electromagnetic ion cyclotron (EMIC) waves [Summers and Thorne, 2003; Albert, 2003], and whistler-mode chorus waves [e.g., Lorentzen et al., 2001; Horne and Thorne, 2003]. Regardless of the precipitation mechanism, these energetic electrons penetrate into the lower ionosphere and mesosphere to altitudes below 85 km to as low as 40–60 km, depending on the energy, and with an energy flux which is 3–4 orders of magnitude greater than the galactic cosmic ray or solar EUV

deposition [Reagan, 1977; Baker et al., 1987, 1993; Gaines et al., 1995]. The rate of energy deposition into the upper atmosphere during intense precipitation events may be as high as  $\sim 10^{19}$ – $10^{20}$  ergs/day [Imhof and Gaines, 1993] and may affect the neutral and ion chemistry of the middle atmosphere [Spear et al., 1984; Callis et al., 1991, 1996, 1997].

[3] Solar particle events (SPE) can also result in the precipitation of energetic ions (0.1 to >100 MeV/nucleon) into the atmosphere. In contrast to energetic electron precipitation events, SPEs occur less frequently but cover the entire polar cap regions down to  $\sim 60^\circ$  magnetic latitude [e.g., Lanzerotti, 1971; Reagan, 1977]. The energy input from the moderate to large SPEs can greatly increase the ionization as well as significantly affecting the neutral chemistry causing large (20–70%) depletions of ozone at high latitudes and mesospheric altitudes [Solomon et al., 1983; Jackman et al., 1993], altering neutral winds [Johnson and Luhmann, 1993], and leading to a cooling of the atmosphere at 45–65 km altitudes [Zadorozhnyy et al., 1992].

[4] VLF sounding (i.e., the measurement of the amplitude and phase of subionospheric signals) is a sensitive tool for the measurement of ionospheric conductivity (i.e., electron density and temperature), especially at altitudes below  $\sim 85$  km, the nighttime reflection height for VLF waves. Precipitating electrons (>50 keV) and protons (>16 MeV) penetrate below 85 km, creating secondary ionization therein as a result of collisions with atmospheric constituents.

<sup>1</sup>Department of Electrical Engineering, Stanford University, Stanford, California, USA.

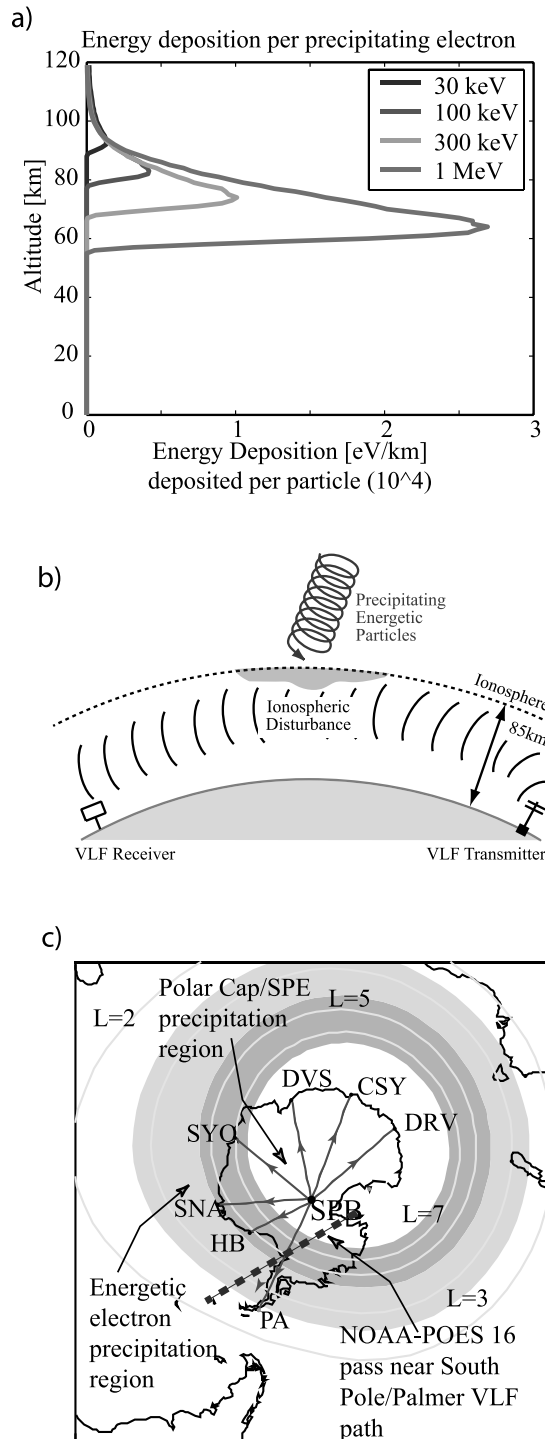


**Figure 1.** (a) Atmospheric energy deposition distributions for electrons of various incident energies, (b) VLF propagation within the Earth-ionosphere waveguide for a path with ionospheric conductivity enhancements owing to energetic particle precipitation, and (c) South Pole beacon experiment showing the location of the South Pole beacon (SPB) and the great circle paths to various receiving sites including Palmer Station (PA). The shaded oval represents the atmospheric entry region of the outer radiation belts.

Figure 1a shows the atmospheric energy deposition as a function of altitude for four different energies of precipitating electrons where the depositions were calculated along the  $L = 7$  field line and each electron had a zero-degree incident pitch angle. The associated changes in ionospheric conductivity along the path cause measurable amplitude and phase changes of the VLF signals propagating in the Earth-ionosphere waveguide as depicted in Figure 1b. Some of the early work on relativistic electron precipitation events has indeed relied on subionospheric VLF measurements [Thorne and Larsen, 1976]. In recent years, the VLF remote sensing method has been extensively utilized to study a variety of lower-ionospheric disturbances owing to energetic electron precipitation such as remote sensing of the auroral electrojet [Cummer *et al.*, 1996; Peter *et al.*, 2006], relativistic electron precipitation enhancements [Cummer *et al.*, 1997; Demirkol *et al.*, 1999], solar proton events [Clilverd *et al.*, 2005, 2006], and lightning-induced electron precipitation (LEP) events [Johnson *et al.*, 1999; Peter and Inan, 2004].

[5] Figure 1c shows the configuration of the South Pole VLF beacon experiment including the VLF great circle paths from the South Pole beacon (SPB) to various receiving locations, including Palmer station (PA) and Halley Bay station (HB). The amplitude and phase of the South Pole beacon VLF transmitter signal observed at the various VLF receivers can be used to detect the magnetic local time (MLT) and  $L$ -shell-dependent disturbances in the  $D$  region ionosphere that overlie or are near the great circle paths between the transmitter and receiver. For example, South Pole station sits within the polar cap region, and hence its great circle path to Palmer station traverses the polar cap, the auroral region, and the outer radiation belts. Halley Bay, with a very similar magnetic longitude to Palmer, has a great circle path from South Pole that traverses the polar cap to just inside the outer radiation belt region. Simultaneous measurements at both of these stations allows for more accurate  $L$ -dependent differentiation of global-scale  $D$  region ionospheric disturbances such as those due to energetic proton precipitation within the polar cap from SPEs or from large-scale precipitation within the outer radiation belts. The transmission schedule of the beacon allows the measurement of temporal variations, albeit relatively coarsely sampled, with 1-min out of every 15-min being the duty cycle used over the course of a 24-h period (owing to power limitations at the South Pole station, the beacon does not transmit continuously). Ionospheric disturbances with time-scales longer than 15 min can be effectively resolved by the beacon experiment. In this manner, VLF remote sensing with the beacon is complementary to precipitation measurements from low orbiting satellites, such as NOAA-POES, which sample a particular geomagnetic region once every 90 min and typically in only one local time region.

[6] The beacon is a 6.7 km horizontal antenna that is elevated above the 3000-m-thick ice sheet at South Pole providing a radiation efficiency of  $\sim 7\%$  at a frequency of 20 kHz, (as opposed to  $<0.1$  percent for the same antenna on conducting ground elsewhere on Earth) [Raghuram *et al.*, 1974]. Therefore during the minute of transmission over the duty cycle, when 6 kW is delivered to the antenna terminals, approximately 420 W is radiated. The current operating frequency is 19.4 kHz, with the antenna wire laid out along the east-west direction, providing a broadside peak of

the radiation pattern in the direction toward Palmer Station. The reception of the beacon signal at Palmer is aided by the relatively low radio frequency interference environment at this exceptionally quiet site.

[7] For the geomagnetically disturbed periods discussed in this paper, Palmer was the only VLF receiver station at which the beacon signal was recorded in wideband fashion, so as to allow coherent integration over a 60-s period, which is necessary to measure both the phase and amplitude of the signal (Halley Bay will be operating with the same receiving system starting in January 2007). The ELF/VLF receiver at Palmer utilizes two orthogonal triangular loop antennas (oriented in the geographic east-west and north-south directions). For the beacon signal propagating geographically northward away from South Pole, the EW loop antenna detects the magnetic field component (along the propagation direction) of the quasi-transverse-electric (QTE) waveguide modes within the Earth-ionosphere waveguide [Budden, 1985]. The NS antenna detects the magnetic field component (transverse to the propagation direction) of the quasi-transverse-magnetic (QTM) modes. The broadband output from each antenna is sent through a preamplifier-line receiver system and is sampled at 100-kHz rate, with GPS-based timing. The system records 3 min of broadband every 15 min, covering the minute before, during, and after that for which the beacon is ON, allowing for the sampling of the local noise levels (at 19.4 kHz) relative to the beacon signal. The amplitude and phase of the beacon signal is determined by taking the Fourier Transform of the broadband signal with an integration time of 60 s (i.e., the entire transmit minute), resulting in a frequency bin width for a 1 min acquisition of 0.03 Hz and thus providing a typical minimum signal-to-noise ratio of >10 dB. It should be noted that all amplitude data measured is absolute, while the phase values are relative. The absolute phase, that is, the total phase difference of the signal received at Palmer relative to the transmitted signal at South Pole, is unknown since we would need to know the phase of the signal along the entire path. Nevertheless, we note that our objective in this paper is to measure the relative variations in the phase of the beacon signal received at Palmer in response to ionospheric changes.

[8] In this paper we present initial results of the observations of ionospheric signatures of energetic particle precipitation enhancements, manifested as variations of the received amplitude and phase of the beacon signal at Palmer Station, Antarctica. We focus on the analysis and modeling of slowly varying (timescales on the order of hours) precipitation enhancements from storms and SPEs during periods in July 2004 and May 2005. To simulate multistation measurements we include modeling predictions of the expected measurements at Halley station if it had been in operation during these periods. Complementary to satellite-based measurements, our results constitute the first step in the establishment of a ground-based system for measuring the ionospheric effects of energetic particle precipitation over Antarctica.

## 2. Received Amplitude and Phase at Palmer Station

[9] It is important to examine the “quiet”-time (little or no energetic particle precipitation) amplitude and phase

measurements of the beacon signal at Palmer before analyzing the measurements during Storms and SPEs so that both seasonal and diurnal variations can be understood.

### 2.1. Day-Night Terminator Effects: Daily and Seasonal Variations

[10] We first examine the beacon signal amplitude and phase as received at Palmer for three different 6-d sequences during geomagnetically quiet times in 2004. The series of data for these periods are displayed as sets in Figure 2, all with the same format. The amplitude and phase data are averaged over 45 min to bring out trends in the midst of more rapid changes. Figure 2a shows the amplitude and phase of the signal measured on the EW magnetic antenna. The amplitude and phase measured by the orthogonal NS oriented antenna are not plotted but show similar behavior. To the right of each amplitude and phase plot are two illustrations displaying the corresponding location (at 85 km altitude) of the day-night terminator at 0420 UT (near magnetic midnight at Palmer) and at 1620 UT (near magnetic noon at Palmer).

[11] Starting with Figure 2a, showing data from early January, we see that the EW phase displays a periodicity with maximum values occurring near 1620 UT while the minimum values are seen near 0420 UT. The phase stays within a band of about 150 degrees. The dashed vertical lines approximately indicate 0420 UT and 1620 UT each day. At both 0420 UT and 1620 UT the great circle path is under a sunlit ionosphere. However, the daytime ionosphere near Palmer at 0420 UT differs from that at 1620 UT owing to the solar ionization rays being more oblique at 0420 UT and thus less penetrating in altitude, thus a change in phase between the two times. It is more difficult to see periodicity in the amplitude data as a result of the terminator effects, since the amplitude is determined by the total absorption integrated along the entire path as well as the effects of waveguide mode interference. The combination of which adds more variance to the received amplitude measurement than that of the phase measurement.

[12] The next sequence shown in Figure 2b is for mid-March, when there is a partial night path to Palmer at 0420 UT and an all daytime path at 1620 UT. This configuration results in even more pronounced periodicity in phase and a larger separation between the extrema, about 200 degrees. In this context, we note that during this period, the beacon transmitter at South Pole remains under daylight conditions. As in January, the March periodicity in the amplitude data is less apparent, and the measured phase shows a more consistent diurnal variation.

[13] The final 6-d sequence, in Figure 2c, captures the response of the system in mid-July when the entire path is in darkness at 0420 UT while only part of it is in darkness at 1620 UT. In both cases the beacon transmitter at South Pole is under a dark ionosphere. As observed on both the EW and NS antenna, the signal phase is somewhat periodic but exhibits more randomness than in the January and March cases. The signal phase generally stays within a 150–200 degree band with a few low swings on days 192 and 193 on both antennas. The fact that much of the great circle path is under darkness for most of the day, and that the nighttime *D* region ionosphere, especially in the auroral

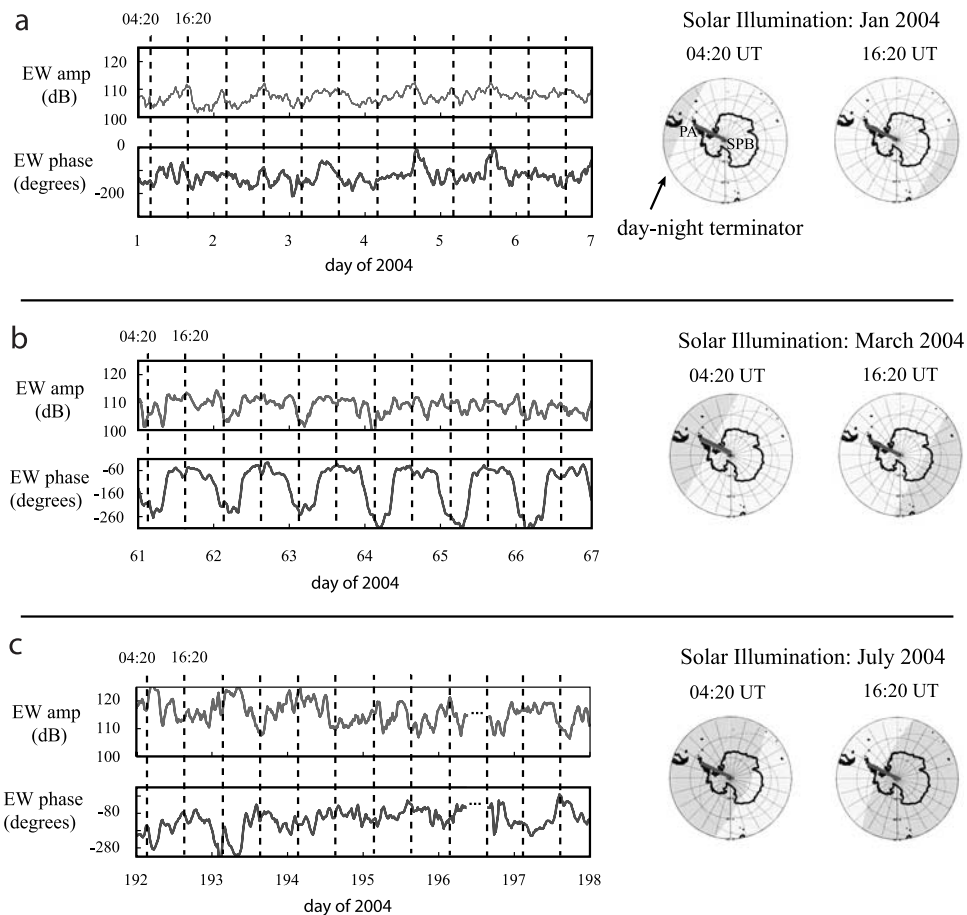


**Figure 2.** Six-day EW antenna amplitude and phase measurements for geomagnetically quiet periods in January 2004, March 2004, and July 2004. The location of the day-night terminator at 85 km (VLF reflection altitude) for 0420 UT and 1620 UT are shown on the corresponding maps with respect to the great circle path between SPB and PA.

regions, exhibits more variation in its electron density profile than it does under daytime conditions, can account for the more random variation in the measured phase. The amplitude data, for both the EW and the NS antennas, exhibits generally higher, albeit noisy, values at 0420 UT than at 1620 UT, thus displaying some periodicity. Furthermore, the amplitudes for this 6-d sequence are, in general, higher than those seen for January and March because of the extended darkness over the path in July, undoubtedly owing to the lower attenuation of VLF waves during nighttime than daytime [Davies, 1966]. The gap in the data on day 196 represents a period when Palmer station was not recording.

[14] When interpreting the effects of energetic particle precipitation and their resultant signatures imprinted in the amplitude and phase data, one must account for the diurnal variation in the received beacon signal occurring at that time of the year for proper analysis and interpretation of signal variations owing to ionospheric changes resulting from storms, substorms, and SPEs. The rest of this paper focuses on geomagnetically disturbed times in July 2004 and May 2005 when the diurnal day-night terminator behavior is that in Figure 2c.

## 2.2. Beacon Signal Amplitude and Phase at Palmer During Two Different Disturbed Periods

[15] We analyze the beacon amplitude and phase measured at Palmer for two geomagnetically disturbed periods. The first period (Case 1) is during July and August of 2004, while the second period (Case 2) is during May of 2005. For both cases the “quiet”-time seasonal and diurnal ionospheric variations are very similar since they both occur about a month from the winter solstice, near day 173. Any difference seen in the amplitude and phase measurements between the two cases are thus associated with the precipitation effects of energetic particles.

[16] Measurements for Case 1 and Case 2 are presented in Figures 3 and 4, respectively. Figures 3 and 4 have identical formats, except for differences in the number of days covered. Figures 3a and 4a display  $Dst$  and serve as a time proxy for the onset of the large-scale geomagnetic disturbances as well as for the injection of energetic particles into the outer radiation belts.

[17] Figures 3b–3d and Figures 4b–4d represent energetic particle measurements for three different particle detectors on the NOAA-POES 16 and 17 satellites as measured by the Space Environment Monitor’s (SEM-2)

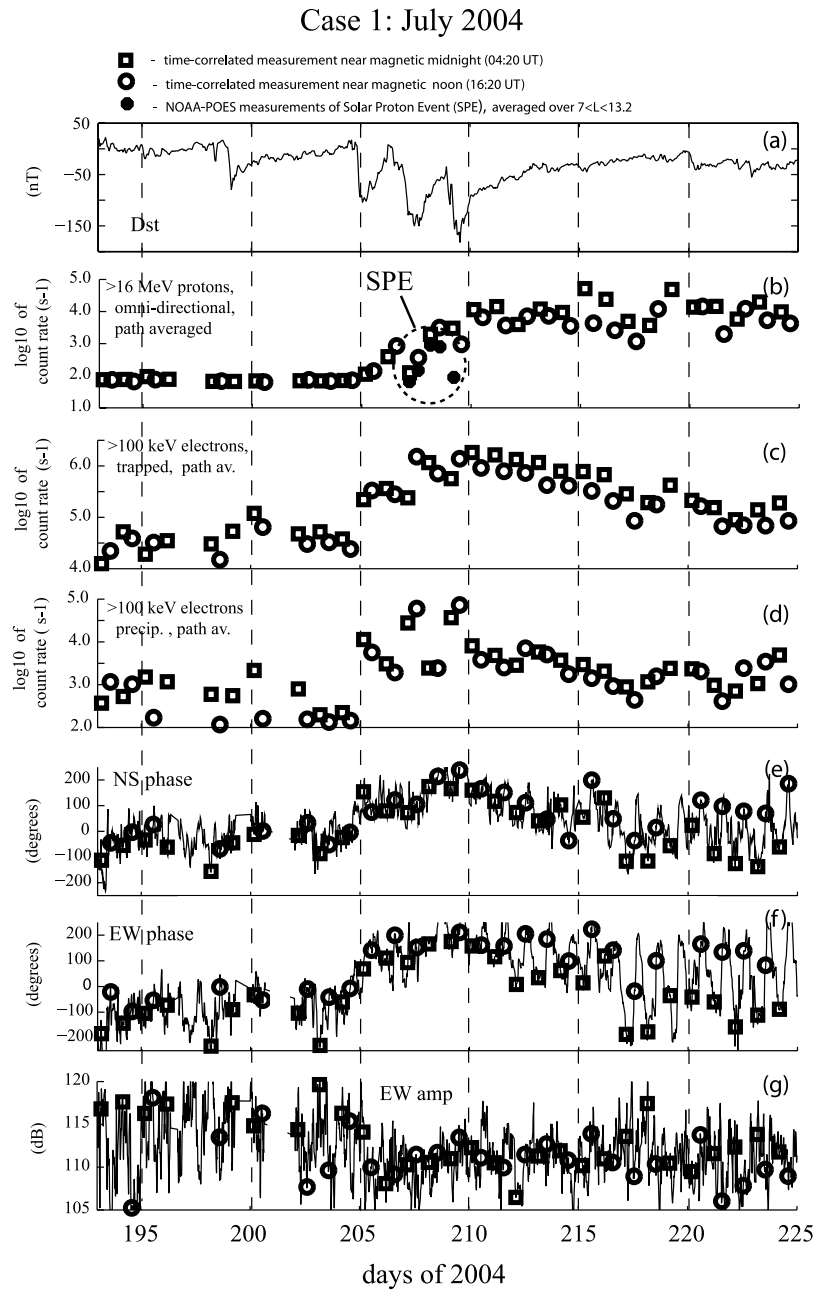


**Figure 3.** Measurements for Case 1, July 2004, including (a) *Dst*. Also shown are NOAA 16,17 POES energetic particle measurements for passes near South Pole to Palmer VLF path for (b) >16 MeV protons, omnidirectional, (c) >100 keV trapped electrons, and (d) >100 keV precipitating electrons, and Palmer measurements of beacon signal for (e) NS antenna phase, (f) EW antenna phase, and (g) EW antenna amplitude.

Medium Energy Proton and Electron Detector (MEPED) instruments. Each data point is a path-averaged count rate measurement. In other words, for a given pass, we average the measured count rate over the  $L$  value range of the South Pole to Palmer VLF path ( $2.49 < L < 13.2$ ), with a sample pass shown in Figure 1c, thus yielding a single path-averaged measurement. This represents a zeroth-order metric to compare with the received VLF signal at Palmer since the received amplitude and phase are affected by precipitation anywhere along the entire path. Each NOAA-POES path-averaged measurement is represented

by either a square, which represent measurements for passes around 0420 UT (magnetic midnight), or a circle, for passes around 1620 UT (magnetic noon). Figures 3b and 4b represent measurements from the omnidirectional detector for >16 MeV protons. The detector cannot differentiate between trapped and precipitating particles and thus mostly represents the trapped population of protons in the outer radiation belts ( $3 < L < 7$ ). However, for both Case 1 and Case 2, solar proton events did occur. These are depicted as black dots and are simply the flux measured by the >16 MeV omnidirectional proton detector averaged over the

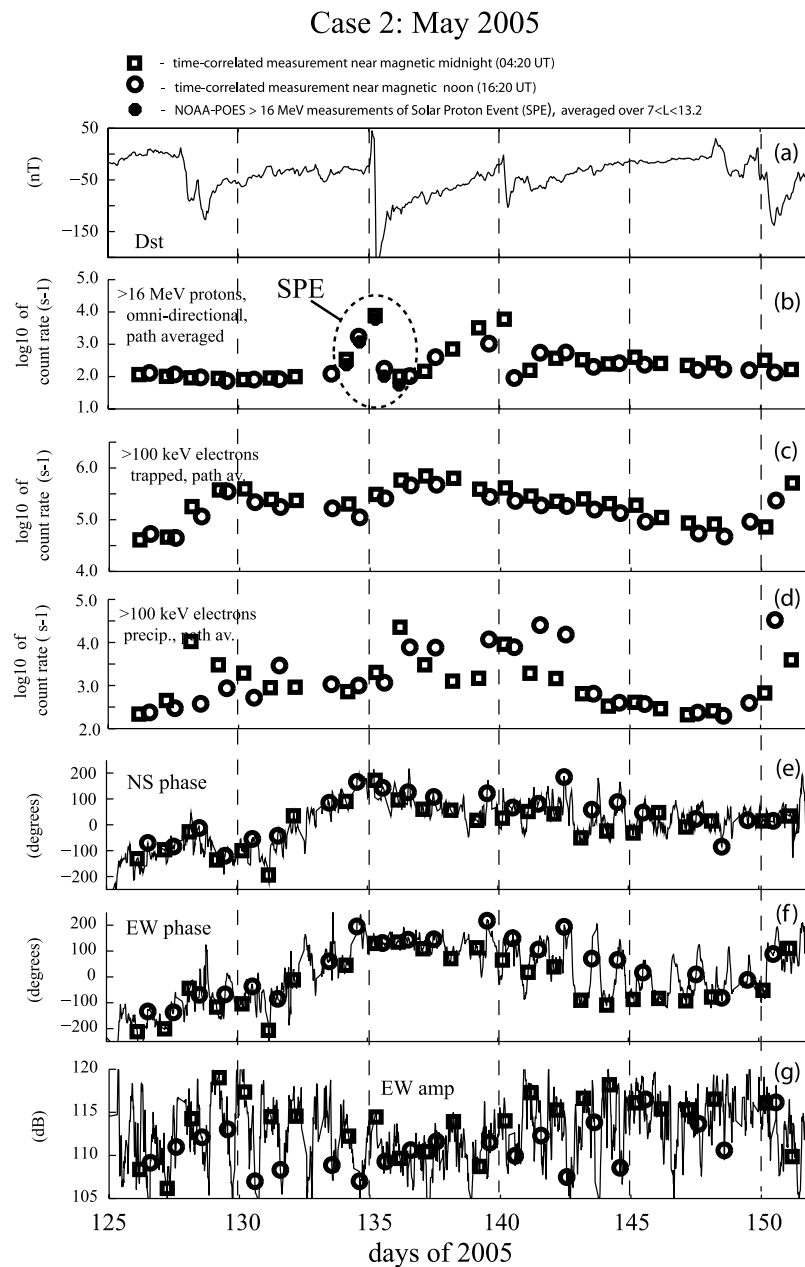


**Figure 4.** Measurements for Case 2, May 2005, including (a) *Dst*. Also shown are NOAA 16,17 POES energetic particle measurements for passes near South Pole to Palmer VLF path, for (b) >16 MeV protons, omnidirectional, (c) >100 keV trapped electrons, and (d) >100 keV precipitating electrons, and Palmer measurements of beacon signal for (e) NS antenna phase, (f) EW antenna phase, and (g) EW antenna amplitude.

$L$  range  $7.0 < L < 13.2$ . The majority of these SPE particles enter the ionosphere on open field lines and precipitate over the polar caps. Figures 3c and 4c represent measurements of the trapped >100 keV electron population. The electron detector is a  $25 \text{ mm}^2$  silicon solid state detector positioned behind a series of metal apertures that define a  $15^\circ$  (half-angle) cone, with the detector oriented typically near  $75$  degrees to the magnetic zenith. The loss cone angle is about  $59^\circ$ , so that the detector for Figures 3c and 4c is located entirely outside the loss cone, thus measuring the trapped flux. Figures 3d and 4d represent measurements of the precipitating >100 keV electrons with the electron

telescope directed at about  $25$  degrees from magnetic zenith, well within the precipitating population at these latitudes. Note that the satellite pass over the  $L$  range of the VLF path typically takes less than  $8$  min, that the precipitating flux levels can vary greatly from seconds to minutes, and that at least part of the pass is at a different magnetic longitude than the VLF path. Thus we are obliged to consider the NOAA-POES data to be a very crude measurement of the precipitation occurring along the VLF path and use the data points to look at trends rather than for one-to-one comparisons with the VLF data.

[18] Figures 3e–3g and 4e–4g show Palmer phase and amplitude measurements of the beacon signal. We plot the full data, that is, measurements every 15 min, which is represented by the grey curve. In addition, the amplitude and phase of the beacon signal at the time of each NOAA-POES measurement (Figures 3b–3d and Figures 4b–4d) is indicated by the associated square or circle. Figures 3e and 3f and Figures 4e and 4f are those of the NS and EW phase, respectively, which are both the least noisy of the beacon measurements. Figures 3g and 4g are the EW amplitude and are generally much noisier than the phase but still show gross trends during the geomagnetic disturbances. The NS amplitude is not shown, since for the cases presented it exhibits very similar behavior to that of the EW amplitude.

### 2.2.1. Case 1: July 2004

[19] In Figure 3a we see a series of three consecutive large drops in  $Dst$  beginning on day 204 near 2000 UT. During this time the  $>16$  MeV proton and the  $>100$  keV electron populations increase dramatically as seen in Figures 3b and 3c, respectively. The second drop in  $Dst$  occurs on day 207 as well as the onset of an SPE that peaks on day 208 and finishes on day 209. The  $>16$  MeV proton population remains high for the rest of the plot. The NOAA-POES  $>6.9$  MeV precipitating proton detector measurements (not shown) exhibit a very similar qualitative behavior as seen in Figure 3b for the  $>16$  MeV omnidirectional flux. After the SPE event, the  $>6.9$  MeV precipitation remains high for the duration of the case period. It is assumed that a portion of the  $>6.9$  MeV precipitating protons are  $>16$  MeV and thus penetrate below the VLF reflection height, affecting VLF propagation.

[20] The trapped  $>100$  keV electron population, Figure 3c, experiences three successive increases corresponding to the three successive drops in  $Dst$  where the population level peaks on day 210 and then gradually decreases in the succeeding days. The precipitating  $>100$  keV electron population, Figure 3d, shows a consistent increase starting on day 204 with some extremely high measurement on day 207 and 209. Once again, the precipitation fluxes are generally more varied than the trapped fluxes, but for the duration of this plot the trends are well behaved, especially after day 205, when the daily measurements at both 0420 UT and 1620 UT are fairly similar.

[21] Strong phase increases in Figures 3e and 3f occur on day 205 that peaks soon after the third drop in  $Dst$  on day 209 and gradually decreases after day 210. By day 217 the phase measured near magnetic midnight (0420 UT) has returned close to prestorm levels while the phase response near magnetic noon (1620 UT) remains high, amounting to an increased diurnal variation in the phase. The diurnal variation is more pronounced in the EW phase than in the NS phase but exhibited by both. A possible explanation for the increased diurnal variations after day 212 begins with the observation that the precipitation measurements in Figure 3d for the  $>100$  keV electrons are quite similar at both magnetic midnight and noon (the same is true for the  $>6.9$  MeV precipitating protons which are not shown). This similarity implies that the differences between the VLF phase responses at 0420 UT versus 1620 UT is due to the VLF propagation effects (i.e., one VLF path is under all night conditions while the other one is partial day, partial

night), since similar levels of precipitation, and thus similar ionospheric enhancements are apparently in effect at both times.

[22] Throughout the duration of the disturbance, the EW amplitude in Figure 3f and the NS amplitude (not shown) remain suppressed. The EW amplitude shows some increased diurnal variation, albeit noisy, mostly after day 217.

### 2.2.2. Case 2: May 2005

[23] For Case 1 the geomagnetic disturbance beginning on day 205 is more or less an isolated event, whereas Case 2 covers a period of three successive moderate to major geomagnetic disturbances, in the middle of which an SPE event occurs. We focus most of our analysis on the second of the three disturbances.

[24] Moderate geomagnetic activity begins on day 127 with a moderate drop in  $Dst$  ( $-100$  nT) and an increase in the  $>100$  keV trapped electron population. The phase generally increases in both the NS and EW antennas during days 127–133.

[25] On day 134 a large solar proton event occurs (Figure 4b), peaking on day 135 and ending on day 136. A large drop in  $Dst$  ( $-210$  nT) occurs near 2000 UT on day 134 and thereafter the  $>100$  keV trapped electron population increases, reaching peak levels which are not as high as those reached in Case 1.

[26] The  $>16$  MeV outer radiation belt proton population (Figure 4b) increases from day 136 to day 140 and then suddenly decreases on day 140 following a moderate ( $-100$  nT) drop in  $Dst$ . After day 140 the population remains higher than pre-SPE levels and slowly decreases over the duration of the plot. The  $>6.9$  MeV precipitating proton measurements (not shown), as in Case 1, show similar qualitative behavior to the  $>16$  MeV omnidirectional flux measurements in Figure 4b. The  $>6.9$  MeV precipitating measurements show an increase from day 135 to 139, then a drop on day 140 and slowly decreasing levels in the succeeding days.

[27] The EW and NS phases exhibit large phase increases during the SPE, both peaking at the peak of the SPE and slowly decreasing thereafter as do the population levels of the trapped proton and electrons. Diurnal variation, strongest in the EW phase, is apparent after day 139, but the effect is not as pronounced as in Case 1, with Case 2 exhibiting smaller diurnal phase swings.

[28] EW amplitude shows a sustained decrease after the onset of the SPE and recovers by day 140. NS amplitude (not shown) shows similar behavior.

[29] The time period ends with another moderate geomagnetic disturbance beginning on day 148. In the next section we model the propagation of the VLF beacon signal to Palmer in the presence of energetic precipitation along the path for various intensities using the measurements from NOAA POES to determine the spatial characteristics of the associated ionospheric disturbance. The model results are then directly compared with the measured amplitude and phase at Palmer.

## 3. Modeling the VLF Beacon Signal Propagation

[30] A comprehensive model is used to relate the observed VLF signal perturbations to the associated ionospheric

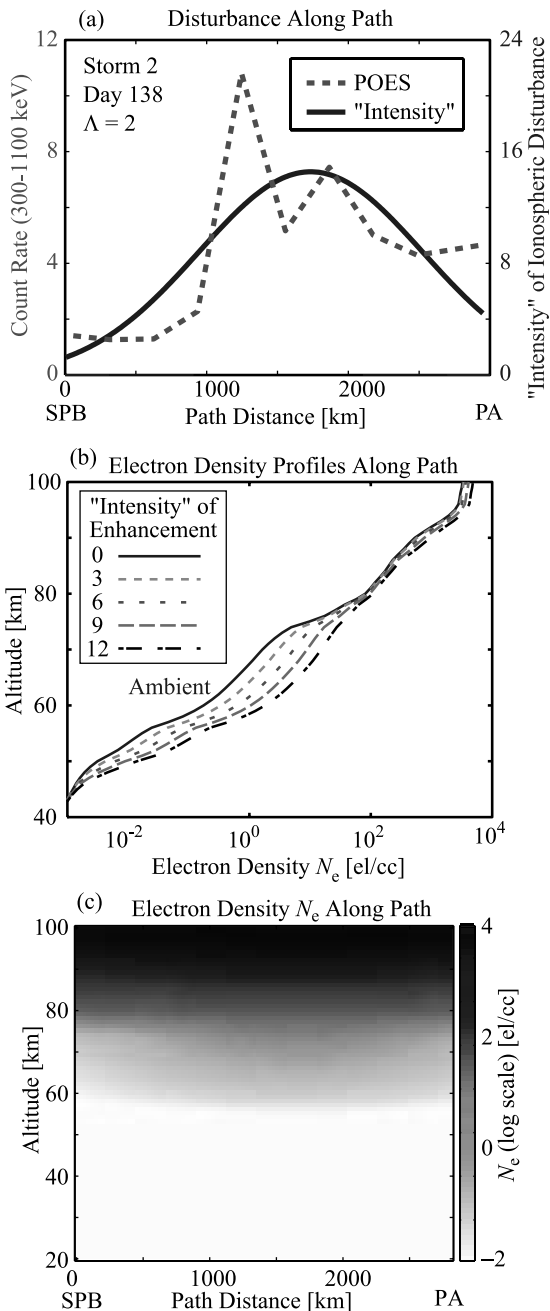


**Figure 5.** Ionospheric density enhancement for (a) NOAA-POES satellite 16-s averaged count rate ( $CR$ ) of precipitating 300–1100 keV electrons (dashed line). The horizontal axis is the distance along the VLF signal path between SPB and PA. A gaussian (solid line) is fitted to the NOAA-POES measurements, used to generate the spatial extent, location, and intensity ( $I$ ) of the ionospheric disturbance input into the model. A conversion ratio ( $\Lambda = I/CR$ ) is used to convert between the NOAA-POES measurements of electron precipitation to the intensity of the ionospheric disturbance. Also shown are (b) electron density profiles sampled along the path with varying “intensities” of enhancement  $I$ , according to the scale shown in Figure 5a, and (c) variation in electron density along the path from SPB to PA input into the model of VLF signal propagation.

disturbance along the VLF signal path. The ionospheric disturbance along the South Pole to Palmer VLF signal path is based on the measurements of precipitation flux made aboard the NOAA-POES satellites. Note that the model includes ionization owing to electrons, but the effects of protons are not currently included in the model. The ionospheric disturbance is then input into a model of VLF subionospheric signal propagation [Chevalier and Inan, 2006], with the model calculations directly comparable to the VLF signal perturbations observed. Through comparison of the model calculations with the VLF observations, the spatial characteristics of the ionospheric disturbances during the two geomagnetic storm periods are examined.

[31] The spatial location and extent of the ionospheric disturbance is based on measurements of energetic electron precipitation made aboard the NOAA-POES 16 and 17 satellites. Figure 5a shows the 16-s averaged count rate ( $CR$ ) of 300–1100 keV electrons as measured by the Space Environment Monitor’s (SEM-2) Medium Energy Proton and Electron Detector (MEPED). The electron telescope is the same as that described previously, with a 25 mm<sup>2</sup> silicon solid state detector positioned behind a series of metal apertures that define a 15° (half-angle) cone. The detector is oriented at about 25 degrees to the earth’s magnetic field line. The horizontal axis is the distance along the VLF signal path between South Pole (SPB) and Palmer (PA). The satellite trajectory is mapped to the VLF signal path, assuming there is no longitudinal variation in the precipitation over the distances considered (typically less than a few degrees). It is assumed that these measurements are representative of the precipitation of energetic electrons into the atmosphere along the VLF signal path. The POES data shown is averaged for all passes occurring between 0400 UT and 0700 UT for both satellites on day 138 of Case 2 (a total of four passes).

[32] For each day modeled, a Gaussian curve is fitted to the NOAA-POES measurements to generate the spatial extent, location, and intensity ( $I$ ) of the ionospheric disturbance used in the model. The fitted Gaussian for day 138 of Case 2 is shown in Figure 5a. It is assumed that the spatial characteristics of the ionospheric disturbance is linearly proportional to the precipitation measured on the NOAA-POES satellites. A conversion ratio ( $\Lambda = I/CR$ ) is used to convert between the NOAA-POES measurements of electron precipitation to the intensity of the ionospheric disturbance. As the pitch angle distribution of the precipitating electrons is unknown, the scale of the ionospheric disturbance resulting for a given precipitation flux (as measured on NOAA-POES) is unknown. Therefore  $\Lambda$  was determined based on comparison of the scale of the model results with the observations.

[33] Perturbed ionospheric electron density profiles for a variety of ‘intensities’ ( $I$ ) of ionospheric disturbance along the VLF signal path are shown in Figure 5b. The variation in altitude of the electron density enhancement is obtained from a Monte Carlo model of energy deposition [Lehtinen, 2000]. The energy spectra were based on the NOAA-POES satellite measurements of 100–300 keV and 300–1100 keV electron precipitation flux. For day 208 of Case 1 and day 138 of Case 2, NOAA-POES detected “harder” energy spectra of precipitation. The energy spectra of the precipi-

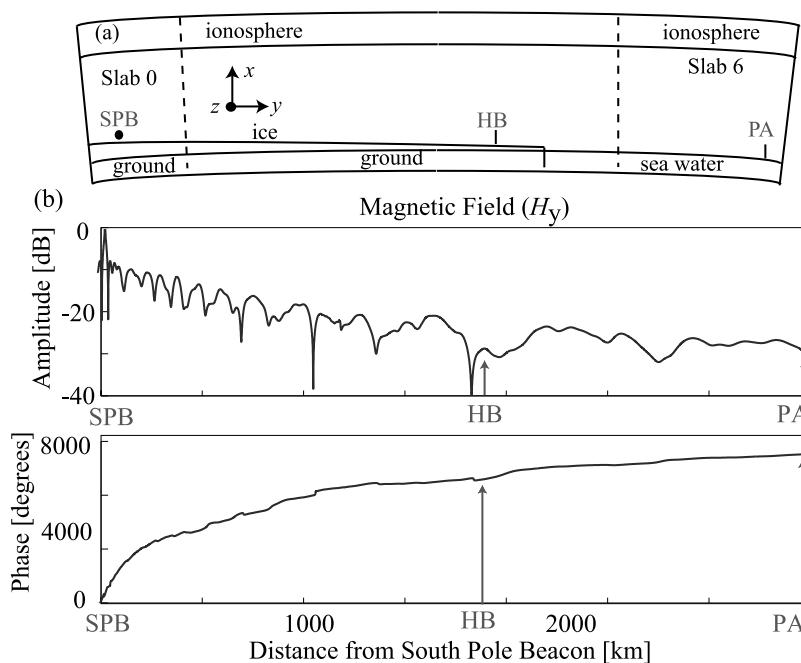


**Figure 6.** Model of VLF signal propagation, showing (a) schematic of the Finite Difference Frequency Domain (FDFD) model of VLF signal propagation, showing the division of the path between the SPB and PA into slabs. The electromagnetic properties of the ice, ground and seawater are included in the model. Also shown are (b) magnetic field  $H_y$  amplitude (top) and phase (bottom) along the GCP from SPB to PA, with respect to the wave magnetic field at SPB, for an ambient ionosphere.

tation used is consistent with the spectra reported by *Gaines et al.* [1995] as measured by the UARS satellite for 14 May 1992 during a period of enhanced geomagnetic activity. For day 207 of Case 1 and day 136 of Case 2, NOAA-POES detected “softer” energy spectra. Input into the Monte Carlo model, this “softer” energy spectra results in an ionospheric disturbance enhancement at generally higher altitudes than for the “harder” energy spectra (see Figure 1a). The “softer” altitude profile of the density enhancement for these 2 d (day 207 of Case 1 and day 136 of Case 2) is similar to that used in the modeling work of LEP events at midlatitudes used in the work of *Peter and Inan* [2007].

[34] Using the ionospheric density profile with altitude obtained from the Monte Carlo model for each night, together with the “intensity” of the ionospheric disturbance as a function of distance along the path (on the basis of the NOAA-POES measurements), the disturbed ionospheric density profile is obtained (Figure 5c). The disturbed ionospheric density along the path is then input into a model of VLF signal propagation.

[35] To quantitatively relate the observed VLF signal perturbations to ionospheric disturbances, we use a finite difference frequency domain (FDFD) model of subionospheric propagation [*Chevalier and Inan*, 2006]. The model consists of a two-dimensional grid in cylindrical coordinates, taking into account the curvature of the Earth. The input parameters into the magnetized plasma equations [*Lee and Kalluri*, 1999] are electron density  $N_e$ , static magnetic field  $B_0$ , and electron-neutral collision frequency  $\mu$ . For the static magnetic field, we apply the tilted dipole model [*Walt*, 1994]. The collision frequency profile can be varied along the path in the model, for the results shown here we use a

constant profile taken from *Ferguson et al.* [1989]. The model also incorporates the electromagnetic properties of ice [*Raghuram et al.*, 1974; *Chevalier et al.*, 2006], seawater, and ground where relevant in the region. Owing to computational resource constraints, the VLF path is broken up into segments, as detailed in Figure 6a, with each segment surrounded with a perfectly matched layer (PML) boundary condition to absorb any outgoing waves [*Chevalier and Inan*, 2004]. Making use of the total field/scattered field methodology [*Taflove and Hagness*, 2000], the VLF signal is propagated from slab-to-slab along the path.

[36] Taking the magnetic field along the surface, the amplitude and phase of the magnetic field along the path is calculated as shown in Figure 6b, with the location of both the Palmer and Halley Bay (HB) receivers shown. Note that we are neglecting longitudinal differences between PA and HB since, as seen in Figure 1c, they are reasonably close in magnetic longitude. Owing to the decay of the higher-order modes with distance, the amplitude and phase of the VLF signal are more stable (i.e., exhibit less variation with distance) at longer distances (i.e., at Palmer).

[37] The conversion ratio  $\Lambda = I/CR$ , which is used to determine the scale of the ionospheric disturbance, was determined by comparing the model results with the observations for a range of  $\Lambda$  (Figure 7). A higher  $\Lambda$  corresponds to a more intense ionospheric disturbance, resulting in a larger phase perturbation of the fields measured by the EW and NS antennas. On the basis of a comparison of the model calculations (solid lines) and the observations (dashed horizontal lines) of the VLF signal perturbations for day 208 of Case 1 and day 138 of Case 2, a  $\Lambda = 10$  is chosen.

[38] The phase and amplitude for the EW and NS antennas at both Palmer and Halley are then calculated using the

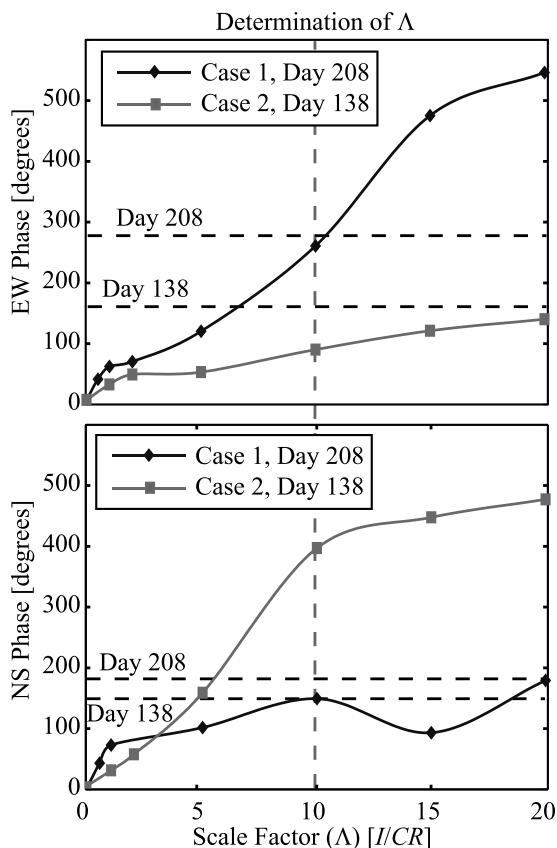


**Figure 7.** Determination of  $\Lambda$  showing modeled VLF phase perturbations at PA versus  $\Lambda$  for day 208 of Case 1 and day 138 of Case 2 (solid lines). The horizontal dashed lines represent the phase perturbations observed on Palmer (averaged over a 3-h period). The phase measurements on day 208 are relative to that on day 202, while those on day 138 are relative to day 130.  $\Lambda$  converts between the NOAA-POES measurements of electron precipitation to the intensity of the ionospheric disturbance on a given day (see Figure 5a). A higher  $\Lambda$  indicates a higher scale for the “intensity” of the ionospheric disturbance, hence resulting in a larger  $\Delta\phi$ . For Figure 8,  $\Lambda$  is set to 10 [I/CR].

model for days 207 and 208 of Case 1 and days 136 and 138 of Case 2 for a  $\Lambda$  of 10 [I/CR]. The modeling results for Palmer and Halley are shown in Figure 8. The model results are compared to the VLF signal perturbations recorded on Palmer, with the amplitude and phase averaged from 0400 to 0700 UT on each night. Coherent phase and amplitude observations are not yet available from Halley.

[39] At Palmer Station, all of the ionospheric disturbances result in a positive phase change in both the  $H_z$  (NS) and  $H_y$  (EW) fields. The phases increase with the increased disturbance associated with the geomagnetic activity, consistent with the observations. For example, on day 208 of Case 1, the model calculates a positive phase change on the EW antenna of 258 degrees, comparable to the phase change of  $\sim 270$  degrees observed. Similarly, on day 136 of Case 2, the model calculates a positive phase change on the NS antenna of 172 degrees, compared to the phase change of  $\sim 220$  degrees observed. The amplitude generally decreases with the onset of geomagnetic activity, also consistent with observations. For example, on day 138 of Case 2, the model calculates an amplitude change of approximately -5 dB for the EW antenna, comparable to the -4 dB change observed. The amplitude and phase response at Halley is more complicated which can be attributed to the presence of higher-order modes (owing to the shorter path).

[40] The general agreement between the Palmer observations and the model calculations suggest that the ionospheric disturbances used in the model reasonably represents the ionospheric conditions at the time of the geomagnetic storms. Differences between the model results and observation may be due to a number of things. There is potential error in the assumed form of the pitch angle and energy distributions of the precipitating electrons. Perhaps fitting a gaussian function to describe the spatial distribution of the disturbance is not valid for all cases nor is excluding the effects of precipitating protons, especially during and after SPE’s. The next addition to the model will be to include the effects of precipitating protons. Current research efforts are underway to characterize the model for a more thorough range of the unknown parameters described above.

**4. Summary**

[41] We have examined the South Pole beacon amplitude and phase data as received at Palmer from the years 2004 and 2005. After presenting the seasonal and diurnal varia-

Case	Day	SPB-PA								SPB-HB			
		Model				Observation				Model			
		EW		NS		EW		NS		EW		NS	
		$\Delta A$	$\Delta\phi$	$\Delta A$	$\Delta\phi$	$\Delta A$	$\Delta\phi$	$\Delta A$	$\Delta\phi$	$\Delta A$	$\Delta\phi$	$\Delta A$	$\Delta\phi$
1	207	-3	53	0	41	-7	190	-4	90	2	35	1	-281
1	208	-9	258	-3	144	-4	270	-4	180	-5	291	-3	227
2	136	-2	100	-2	172	-5	220	-7	200	0	-212	13	-208
2	138	-5	84	-12	395	-4	160	-3	150	-13	195	-6	128

**Figure 8.** Model calculations compared to observations of VLF signal perturbations. The amplitude and phase perturbations for Case 1 are relative to the amplitude and phase measured on day 202, while those on Case 2 are relative to the amplitude and phase measured on day 130. The observed amplitude and phase perturbations are averaged over a 3-h period from 0400 to 0700 UT. Observations are not available for SPB-HB.

tions based on the location of the day/night terminator, we focused on two periods of time with high magnetic activity. The observed amplitude and phase measurements of the beacon signal at Palmer coincides with increased relativistic electron and proton flux as recorded on the MEPED instrument aboard the NOAA-16 and 17 POES satellites. An FDFD model of the propagation of the VLF signal based on an ionosphere derived from the MEPED electron data and a Monte Carlo atmospheric model of energy deposition reproduces the general trends seen at Palmer.

[42] Our results constitute the first step in the establishment of a new ground-based system for measurement of the ionospheric effects of relativistic particle precipitation over Antarctica, in a manner complementary to satellite-based measurements.

[43] Current and future research efforts consist of the inclusion of additional beacon signal measurement sites such as Halley. For the model, the inclusion of the effects of proton ionization is a next step in the ionospheric conductivity model as was done by Clilverd *et al.* [2005]. Finally, the investigation of more isolated ionospheric disturbance events due strictly to energetic electron precipitation, which typically occur during substorms, is currently underway.

[44] **Acknowledgments.** We are grateful to Dave Evans from NOAA for his help with the NOAA-16 and 17 POES data. We would like to thank Don Carpenter for reading and valuable comments on the manuscript. This research was sponsored by the Office of Polar Programs of NSF under grant OPP-0093381-001. The collection of the Palmer VLF data was sponsored by the Office of Polar Programs of NSF under grant OPP-0233955.

[45] Amitava Bhatnagar thanks J. Semeter, Karl-Heinz Glassmeier, and another reviewer for their assistance in evaluating this paper.

## References

- Albert, J. M. (2003), Evaluation of quasi-linear diffusion coefficients for EMIC waves in a multispecies plasma, *J. Geophys. Res.*, *108*(A6), 1249, doi:10.1029/2002JA009792.
- Baker, D. N., J. B. Blake, R. W. Klebesadel, and P. R. Higbie (1986), Highly relativistic electrons in the Earth's outer magnetosphere: 1. Lifetimes and temporal history 1979–1984, *J. Geophys. Res.*, *91*, 4265.
- Baker, D. N., R. C. Anderson, R. D. Zwickl, and J. A. Slavin (1987), Average plasma and magnetic field variations in the distant magnetotail associated with near-Earth substorm effects, *J. Geophys. Res.*, *92*, 71.
- Baker, D. N., R. A. Goldberg, F. A. Herrero, J. B. Blake, and L. B. Callis (1993), Satellite and rocket studies of relativistic electrons and their influence on the middle atmosphere, *J. Atmos. Terr. Phys.*, *55*, 1619.
- Budden, K. G. (1985), *The Propagation of Radio Waves*, Cambridge Univ., Cambridge.
- Callis, L. B., D. N. Baker, J. B. Blake, J. D. Lambeth, R. E. Boughner, M. Natarajan, R. W. Klebesadel, and D. J. Gorney (1991), Precipitating relativistic electrons; their long-term effect on stratospheric odd nitrogen, *J. Geophys. Res.*, *96*, 2939.
- Callis, L. B., R. E. Boughner, D. N. Baker, R. A. Mewaldt, J. B. Blake, R. S. Selesnick, J. R. Cummings, M. Natarajan, G. M. Mason, and J. E. Mazur (1996), Precipitating electrons: Evidence for effects on mesospheric odd nitrogen, *Geophys. Res. Lett.*, *23*, 1901.
- Callis, L. B., M. Natarajan, J. D. Lambeth, and R. E. Boughner (1997), On the origin of midlatitude ozone changes: Data analysis and simulations for 1979–1993, *J. Geophys. Res.*, *102*, 1215.
- Chevalier, M. W., and U. S. Inan (2004), A PML using a convolutional curl operator and a numerical reflection coefficient for general linear media, *IEEE Trans. Ant. Propag.*, *2*(7), 1647.
- Chevalier, M. W., and U. S. Inan (2006), A technique for efficiently modeling long path propagation for use in both FDFD and FDTD, *IEEE Antennas Wireless Propag. Lett.*, *5*(1), 525–528.
- Chevalier, T. W., U. S. Inan, and T. F. Bell (2006), Characterization of terminal impedance and radiation properties of a horizontal VLF antenna over Antarctic ice, *Radio Sci.*, *41*, RS6001, doi:10.1029/2005RS003298.
- Clilverd, M. A., C. J. Rodger, T. Ulich, A. Seppala, E. Turunen, A. Botman, and N. R. Thomson (2005), Modeling a large solar proton event in the southern polar atmosphere, *J. Geophys. Res.*, *110*, A09307, doi:10.1029/2004JA010922.
- Clilverd, M. A., A. Seppala, C. J. Rodger, N. R. Thomson, P. T. Verronen, E. Turunen, T. Ulich, J. Lichtenberger, and P. Steinback (2006), Modeling polar ionospheric effects during the October–November 2003 solar proton events, *Radio Sci.*, *41*, RS2001, doi:10.1029/2005RS003290.
- Cummer, S. A., T. F. Bell, U. S. Inan, and L. J. Zanetti (1996), VLF remote sensing of the auroral electrojet, *J. Geophys. Res.*, *101*, 5381.
- Cummer, S. A., T. F. Bell, and U. S. Inan (1997), VLF remote sensing of high-energy auroral particle precipitation, *J. Geophys. Res.*, *102*, 7477.
- Davies, K. (1966), *Ionospheric Radio Propagation*, Dover, New York.
- Demirkol, M. K., U. S. Inan, T. F. Bell, S. G. Kanekal, and D. C. Wilkinson (1999), Ionospheric effects of relativistic electron enhancement events, *Geophys. Res. Lett.*, *26*, 3557.
- Ferguson, J. A., F. P. Snyder, D. G. Morfitt, and C. H. Shellman (1989), Long-wave propagation capability and documentation, *Tech. Doc. 1518*, Naval Ocean Syst. Cent., San Diego, Calif.
- Gaines, E. E., D. L. Chenette, W. L. Imhof, C. H. Jackman, and J. D. Winningham (1995), Relativistic electron fluxes in May 1992 and their effect on the middle atmosphere, *J. Geophys. Res.*, *100*, 1027.
- Green, J. C., T. G. Onsager, T. P. O'Brien, and D. N. Baker (2004), Testing loss mechanisms capable of rapidly depleting relativistic electron flux in the Earth's outer radiation belt, *J. Geophys. Res.*, *109*, A12211, doi:10.1029/2004JA010579.
- Horne, R. B., and R. M. Thorne (2000), Electron pitch angle diffusion by electrostatic electron cyclotron harmonic waves: The origin of pancake distributions, *J. Geophys. Res.*, *105*(A3), 5391.
- Horne, R. B., and R. M. Thorne (2003), Relativistic electron acceleration and precipitation during resonant interactions with whistler-mode chorus, *Geophys. Res. Lett.*, *30*(10), 1527, doi:10.1029/2003GL016973.
- Imhof, W. L., and E. E. Gaines (1993), Inputs to the atmosphere from relativistic electrons, *J. Geophys. Res.*, *98*, 13,575.
- Jackman, C. H., J. E. Nielsen, and D. J. Allen (1993), The effects of the October 1989 solar events on the stratosphere as computed using a three-dimensional model, *Geophys. Res. Lett.*, *20*, 459.
- Johnson, M. P., U. S. Inan, and D. S. Lauben (1999), Subionospheric vlf signatures of oblique (nonducted) whistler-induced precipitation, *Geophys. Res. Lett.*, *26*, 3569.
- Johnson, R. M., and J. G. Luhmann (1993), Poker flat MST observations of high latitude neutral winds at the mesopause during and after solar proton events, *J. Atmos. Terr. Phys.*, *55*, 1203.
- Lanzerotti, L. J. (1971), Equatorial and precipitating solar protons in the magnetosphere: 1. Low-energy diurnal variations, *J. Geophys. Res.*, *76*, 5235.
- Lee, J. H., and D. K. Kalluri (1999), Three-dimensional FDTD simulation of electromagnetic wave transformation in a dynamic inhomogeneous magnetized plasma, *IEEE Trans. Antennas Propag.*, *47*(7), 1146.
- Lehtinen, N. G. (2000), Relativistic runaway electrons above thunderstorms, dissertation, Stanford Univ., Stanford, Calif.
- Lorentzen, K. R., J. B. Blake, U. S. Inan, and J. Bortnik (2001), Observations of relativistic electron microbursts in association with VLF chorus, *J. Geophys. Res.*, *106*, 6017.
- Paulikas, G. A., and J. B. Blake (1979), Effects of the solar wind on magnetospheric dynamics: Energetic electrons at the synchronous orbit, in *Quantitative Modeling of Magnetospheric Processes*, *Geophys. Monogr. Ser.*, vol. 21, edited by W. P. Olson, pp. 180–202, AGU, Washington, D. C.
- Peter, W. B., and U. S. Inan (2004), On the occurrence and spatial extent of electron precipitation induced by oblique nonducted whistler waves, *J. Geophys. Res.*, *109*, A12215, doi:10.1029/2004JA010412.
- Peter, W. B., and U. S. Inan (2007), Quantitative comparison of lightning-induced electron precipitation via VLF remote sensing, *J. Geophys. Res.*, doi:10.1029/2006JA012165, in press.
- Peter, W. B., M. W. Chevalier, and U. S. Inan (2006), Perturbations of midlatitude subionospheric VLF signals associated with lower ionospheric disturbances during major geomagnetic storms, *J. Geophys. Res.*, *111*, A03301, doi:10.1029/2005JA011346.
- Raghuram, R., R. L. Smith, and T. F. Bell (1974), VLF Antarctic antenna: Impedance and efficiency, *IEEE Trans. Antennas Propag.*, *22*, 318.
- Reagan, J. B. (1977), Ionization processes, in *Dynamical and Chemical Coupling*, edited by B. Grandal and J. A. Holtet, p. 145, D. Reidel, Dordrecht, Holland.
- Solomon, S., G. C. Reid, D. W. Rusch, and R. J. Thomas (1983), Mesospheric ozone depletion during the solar proton event of July 13, 1982, II, Comparison between theory and measurement, *Geophys. Res. Lett.*, *10*, 257.
- Spear, K. A., S. Solomon, R. J. Thomas, and D. W. Rusch (1984), Mesospheric response to particle precipitation (abstract), *Eos Trans. AGU*, *65*, 1029.
- Summers, D., and R. M. Thorne (2003), Relativistic electron pitch-angle scattering by electromagnetic ion cyclotron waves during geomagnetic storms, *J. Geophys. Res.*, *108*(A4), 1143, doi:10.1029/2002JA009489.

- Summers, D., R. M. Thorne, and F. Xiao (1998), Relativistic theory of wave-particle resonant diffusion with application to electron acceleration in the magnetosphere, *J. Geophys. Res.*, *103*, 20,487.
- Taflove, A., and S. C. Hagness (2000), *Computational Electrodynamics: The Finite-Difference Time-Domain Method*, Artech House, Boston.
- Thorne, R. M., and T. R. Larsen (1976), An investigation of relativistic electron precipitation events and their association with magnetospheric substorm activity, *J. Geophys. Res.*, *81*, 5501.
- Walt, M. (1994), *Introduction to Geomagnetically Trapped Radiation*, Cambridge Univ. Press, New York.
- Zadorozhnyy, A. M., V. N. Kikhthenko, G. A. Kokin, O. M. Raspopov, O. V. Shumilov, G. A. Tuchkov, M. I. Tyasto, A. F. Chizhov, and O. V. Shtyrkov (1992), The reaction of the middle atmosphere to solar proton events in October 1989, *Geomagn. Aeron.*, *32*, 184.
- Zhao, Y.-J., K.-L. Wu, and K.-K. M. Cheng (2002), A compact 2-D full-wave finite-difference frequency-domain method for general guided wave structures, *IEEE Trans. Microwave Theory Tech.*, *50*, 1844.
- 
- T. F. Bell, M. W. Chevalier, U. S. Inan, W. B. Peter, and M. Spasojevic, Department of Electrical Engineering, Stanford University, 351 Packard EE Building, Stanford, CA 94103, USA. (chamonix@stanford.edu)